JGR Planets

RESEARCH ARTICLE

10.1029/2020JE006748

Key Points:

- We interpret an igneous provenance to mounds and ridges at the center of a floor fractured crater in Arabia Terra
- The igneous ridge-mound assemblies follow the orientation of linear tectonic features in Arabia Terra
- The studied crater represents a new class of diminutive volcanic centers in Arabia Terra resulting from tectono-volcanism

Supporting Information:

Supporting Information may be found in the online version of this article.

Correspondence to:

A. Basu Sarbadhikari,
amitbs@prl.res.in

Citation:

Rani, A., Basu Sarbadhikari, A., Sinha, R., Karunatillake, S., Komatsu, G., & Bates, A. (2021). Evidence of regionally distributed tectono-volcanism in a floor fractured crater of North-Central Arabia Terra, Mars. *Journal of Geophysical Research: Planets*, *126*, e2020JE006748. https://doi.org/10.1029/2020JE006748

Received 26 OCT 2020
Accepted 6 OCT 2021

Evidence of Regionally Distributed Tectono-Volcanism in a Floor Fractured Crater of North-Central Arabia Terra, Mars

A. Rani[1,2], A. Basu Sarbadhikari[1], R. Sinha[1,2], S. Karunatillake[3], G. Komatsu[4], and A. Bates[3]

[1]Physical Research Laboratory, Ahmedabad, India, [2]Indian Institute of Technology, Gandhinagar, India, [3]Department of Geology and Geophysics, Louisiana State University, Baton Rouge, LA, USA, [4]International Research School of Planetary Sciences, Università d'Annunzio, Pescara, Italy

Abstract Arabia Terra features many tectonic structures, which have been correlated to episodes of incipient tectonics, massive impacts, and controls on fluvial systems. However, the extent of regionally distributed tectono-volcanism and its effects on local structures remains unknown. To characterize the prevalence of volcanically driven processes in this region, we investigate the geomorphic features of an unnamed ~85-km diameter and 3.6 Ga old floor-fractured crater (FFC) in North-Central Arabia Terra. Widespread crater floor rocks resemble layered sedimentary deposits. Nevertheless, the central crater floor hosts mounds and linear ridges, which have higher thermal inertia than the surroundings, indicating a provenance distinct from the sedimentary units. Crosscutting relationships suggest that the mounds and ridges are stratigraphically overlying the layered sedimentary rocks. Morphologically and morphometrically, the mounds and ridges resemble known Martian and terrestrial volcanic cone and dike systems. Unlike other FFCs of Arabia Terra, the dikes and cone azimuths consistently orient in the NW-SE direction, implying that regional tectonic controls on their formation overrode localized effects of the crater-forming impact. Our observations collectively support magma intruding and erupting along regionally controlled tectonic structures; the migration of magma was perhaps facilitated by the impact that formed the host crater. Consequently, the studied FFC may represent a category of hitherto unrecognized numerous small-scale volcanic centers controlled by regional tectono-volcanism within Arabia Terra. This is also consistent with regionally distributed magmatic systems in the late Noachian to early Hesperian, associated with a thermally eroded crust.

Plain Language Summary The highly cratered plain of Arabia Terra is one of the oldest provinces of Mars and is situated at an important geologic division between the Martian highlands and lowlands. Northern Arabia Terra has been reported for preserved plain-style caldera complexes, which resemble terrestrial supervolcanic calderas. In this context, we discuss previously unrecognized evidence of intrusive igneous process at the center of a floor-fractured crater (FFC) in North-Central Arabia Terra. We consider whether the observed geomorphic features are related to impact cratering or to regional intrusive activity during the late Noachian-early Hesperian. Our study reveals the existence of volcanic cones and dikes within the central floor of the crater. We also observe a preferred orientation of the igneous features, which shows a parallel alignment to regional linear tectonic features. We suggest that the igneous intrusions within the FFC were controlled preferably along the preexisting weak planes (i.e., faults) in response to the regional tectonism, while the magmatism was primarily triggered by the FFC-forming impact event. These findings shed new light on the regionally distributed magmatic systems within Arabia Terra during the late Noachian and early Hesperian.

1. Introduction

Arabia Terra, as characterized by crater size-frequency dating (Michael, 2013) and geological mapping (Tanaka et al., 2014), dates to the Late to Mid Noachian, making it one of the oldest terrains on Mars. Past studies suggest that Arabia Terra experienced extensive surface modification (Hynek & Phillips, 2001; McGill, 2000) by glacial (Carr, 1986; Zeilnhofer et al., 2018), fluvial (Davis et al., 2016; Dohm et al., 2007), massive impact (Dohm et al., 2007), aeolian (Rodriguez et al., 2010; Silvestro et al., 2011), tectonic (Anguita

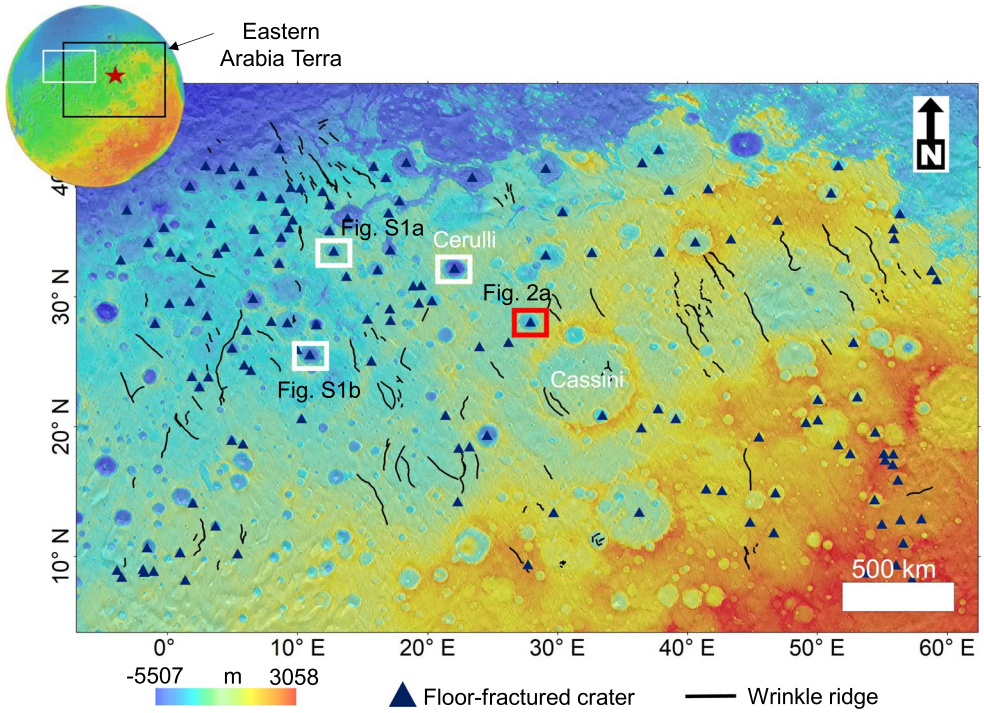

Figure 1. Thermal Emission Imaging System daytime Infrared basemap of eastern Arabia Terra region overlain by color coded Mars Orbiter Laser Altimeter and High-Resolution Stereo Camera topographic map (location of Eastern Arabia Terra marked by a black box in global map at the upper left), showing distributions of floor-fractured craters (FFCs; after Bamberg et al., 2014) and wrinkle ridges. The white box in global inset map indicates the study area of Michalski and Bleacher (2013). The unnamed FFC of this study is marked by a red box and a red star in Mars globe. Blue boxes demarcate other FFCs (only two are shown in Figure S1 in Supporting Information S1, as example), which abundantly present in Arabia Terra.

et al., 1997), and hydrothermal processes (Noe Dobrea et al., 2010; Oehler & Allen, 2010). The broad range of process interpretations at times contradict each other, warranting a further study of Arabia to gain insight into its evolution.

The densely cratered landscape of Arabia Terra (Greeley & Guest, 1987) is broadly characterized as having a relatively thin crust (Neumann et al., 2004). Over this thin crust, a large fraction (more than 50% of Mars) of floor-fractured craters (FFCs) have been identified (Bamberg et al., 2014; Schultz & Glicken, 1979) (Figures 1 and S1 in Supporting Information S1). This thin crust features numerous wrinkle ridges (Figure 1), indicating a regional-scale tectonism (Anderson et al., 2008; Bamberg et al., 2014; Dohm et al., 2002; Golombek et al., 2001). Similarities in wrinkle ridge orientations span from southwestern Arabia Terra on Noachian ridged plateau unit (Greeley & Guest, 1987) to Northwestern Arabia Terra near a possible instance of ancient intense magmatism (Bates et al., 2020; Michalski & Bleacher, 2013; Whelley et al., 2021). The nature of these wrinkle ridges in context with regional magma bodies intruding tectonically driven faults (i.e., tectono-magmatism) remain unclear. Our work attempts to correlate the igneous features within a roughly 3.6 Ga old crater to a said regional tectono-magmatism.

We pursue a case study in the north-central region of Arabia Terra, with specific focus on an impact crater, which we consider a type example for igneous features formed through the regional tectono-magmatism. Our detailed geological investigation within Arabia Terra (geographic extent: 44°N to 8°N and −4°E to 60°E) characterizes the distribution and orientation of wrinkle ridges in a regional context (Figure 1). For local insight into geologic processes, we morphologically and structurally characterize an ~85-km diameter FFC, centered at 28°N, 28°E. This FFC contains preserved ridges, mounds, mesas, and layered sedimentary rocks within the central floor of the crater, which resides in the North-Central Arabia Terra region (Figures 2a and 2b; Rani et al., 2020; Schultz & Glicken, 1979). Taken together, the observations reported in this study help to characterize the possibility of regional tectono-magmatism within Arabia Terra.

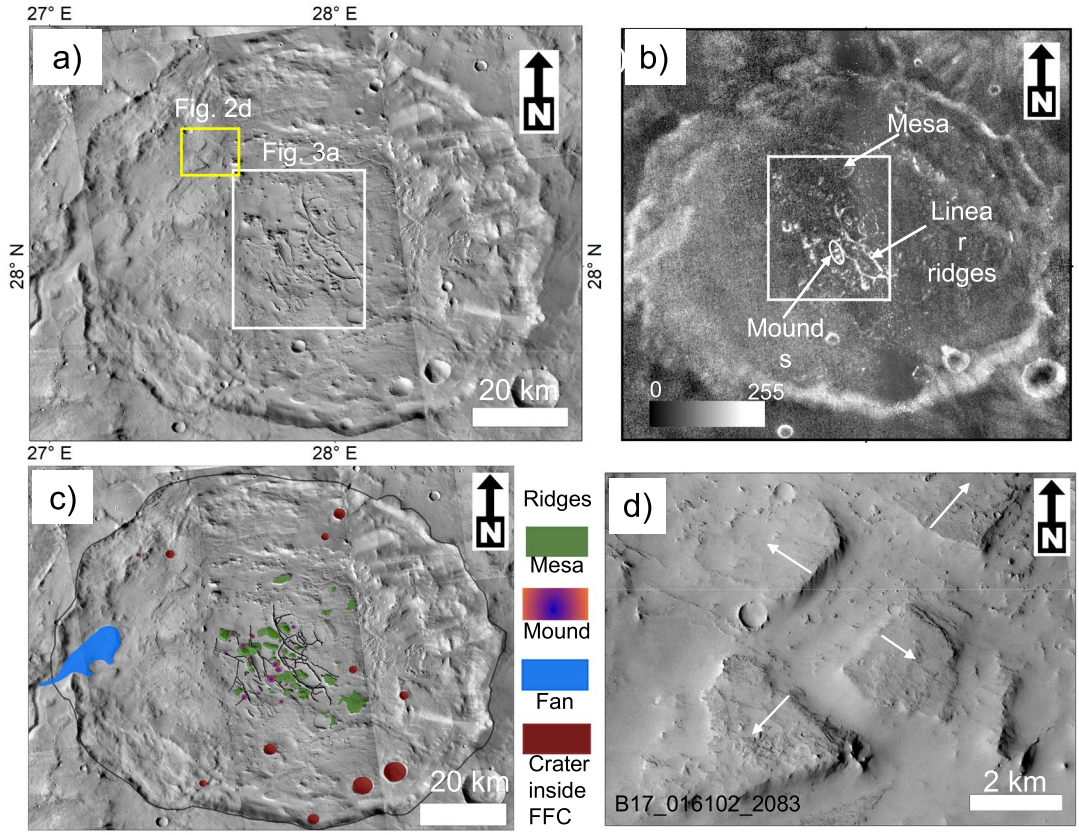

Figure 2. (a) Magnified view of the study crater using Context Camera (CTX) images. The white box is the central part of the crater with a distinct geomorphology shown in Figure 3a, and the yellow box represents the crater floor features outside the central part. (b) Thermal Emission Imaging System nighttime Infrared image illustrates the material property of different landforms within the crater. (c) CTX image-based geomorphic map of the study crater at a 1:15,000 scale with the crater boundary marked by a solid black line. The legend is shown at the right side with different relevant landforms present inside the crater. (d) Mesas at the outside part of the crater floor are displaced from each other by fractures. Four blocks were plausibly the parts of a single unit close to the crater rim wall, indicating a floor-fracture crater. Arrows mark the displacement direction of the adjacent blocks (CTX image credit: NASA/JPL-Caltech/MSSS).

2. Data and Methods

We use Mars Reconnaissance Orbiter (MRO) Context Camera (CTX; ~6 m/pixel; Malin et al., 2007) images of Arabia Terra to identify the geomorphic features (i.e., linear and wrinkle ridges, mounds, etc.) inside and outside the study crater using ArcMap 10.0 (Environmental Systems Research Institute, Inc. Redlands, CA, USA). MRO High-Resolution Imaging Science Experiment (HiRISE; ~0.25 cm/pixel; McEwen et al., 2007) images are used to identify the boulders at flanks of ridges because the boulders are generally larger than the resolution of HiRISE, but smaller than the resolution of CTX. For the detailed topographic investigation of morphological units identified inside the study crater, CTX and HiRISE stereo imagery is used for generating Digital Terrain Models (DTMs) (Malin et al., 2007; Shean et al., 2011). The built-in pipelines of the Mars Information System (MarsSI) are used to process the CTX and HiRISE stereo imagery and to create the DTMs (Lozac'h et al., 2015; Quantin-Nataf et al., 2018). One CTX and two HiRISE stereo image pair, mainly covering the central portion of the crater, is available for the study crater.

To characterize and correlate the linear geologic features (i.e., ridges) of the study crater with any regional tectonism that may have been active in the past, we plot the orientations of the linear features in rose diagram. Topographic variability of the North-Central Arabia Terra is analyzed using Mars Orbiter Laser Altimeter and High-Resolution Stereo Camera (MOLA-HRSC) blended Digital Elevation Model (DEM) data (spatial resolution ~200 m/pixel) (Fergason et al., 2018).

Using HiRISE DTM, we calculate height, width, length, and spacing of the ridges and generate slope maps. We also calculate the slope angle of the ridges by dividing the height with width to depict the steepness of ridges. The orientation of the linear ridges is calculated by weighing the direction with the length, which represents the vector quantity that can be computed as the azimuth in rose diagram. Using CTX DTM data, we estimate mound morphometry with average height (H), average basal diameter (W), and average flank slope (α). Highly degraded and very small-sized mounds of a few tens of meters in height (<50 m) are excluded from the morphometric calculations. Mound height is calculated by subtracting the values of the surrounding areas adjacent to the mound (determined from MOLA data) from the maximum elevation point. The errors in measuring the average basal diameter and average mound height are estimated by dividing the mean by deviation from the least squares best fit. The slope of each of the mounds (α_z) is manually calculated by the numerical differentiation of a cone's shape using the following formula

$$\alpha_z\left(h\right) = 0.1\int_{h-0.05}^{h+0.05} \alpha\left(h'\right)dh' \tag{1}$$

where $h = \dfrac{z - z_0}{z_1 - z_0}$, $h \in \left\langle 0.05, 0.95 \right\rangle$; z_0 corresponds to the zero height i.e., base level; and z_1 corresponds to maximum height (after Brož et al., 2015).

To examine the correlations in the spatial distributions of mounds, we use a two-point azimuth technique, within ArcGIS, which measures the alignment of the mounds relative to each other (Bleacher et al., 2009; Connor & Conway, 2000; Lutz, 1986; Roberts et al., 2011). The method that most accurately captures the spatial correlations of mounds involves representing mounds as points in space through the use of probabilistic lattice point distributions (Wadge & Cross, 1988). As the paleo-propagation direction of the mounds is unknown, we use the acute angle between each connecting line segment of the mounds and an imaginary geographic N-S line as the azimuth. This technique has been widely used to quantify trends within the structural geology of igneous mounds and vents at varying scales, from tens of meters to thousands of kilometers, which makes it ideal for this study (Bleacher et al., 2009; Roberts et al., 2011; Wadge & Cross, 1988).

We also characterize thermal inertia (TI) of different surface materials on the studied features using the Thermal Emission Imaging System (THEMIS) onboard Mars Odyssey. We use a qualitative THEMIS Infrared (IR; ~100 m/pixel) nighttime imagery (THEMIS_TI_Mosaic_Quant_00N000E, band 9, transparent to the atmosphere, absolute accuracy ~1 K) to calculate TI (Christensen et al., 2003; Fergason et al., 2006). Nighttime, especially predawn IR images intrinsically depend on material properties, show little or no effect from albedo, and are minimally affected by a topographic variation (Cushing et al., 2009). The nature of the surface materials, such as hard rock or soft unconsolidated sand or dust, can be distinguished using the range of values from THEMIS_TI data. We use this relationship to distinguish the different geomorphic units as well as dust-covered surfaces.

3. Results of the FFC Case Study

The thermal nighttime image (THEMIS_TI) provides data for thermophysical analysis of the various landforms observed in the high-resolution visible wavelength images by CTX and HiRISE. The geomorphic features at the central portion of the crater (linear ridges and mounds; Figure 2a) have higher TI values (~140 $Jm^{-2}K^{-1}s^{-1/2}$) relative to the surroundings (~40 $Jm^{-2}K^{-1}s^{-1/2}$) (Figure 2b). The linear ridges and mounds have considerably higher TI values than the equally elevated landform mesas (40–45 $Jm^{-2}K^{-1}s^{-1/2}$). In the nighttime THEMIS IR image, the linear ridges and mounds of FFC stand out brightly from the surrounding landscape, namely mesa and sedimentary layers (Figure 2b). Relative to FFC's immediate surroundings, these values are significantly high, although this area is generally dust obscured (Amador et al., 2010; Farrand et al., 2005; Williams et al., 2018).

The ~85-km diameter FFC (Figure 2a) has degraded considerably. The numerical model age of the crater as calculated by the least-squares fit age using a crater size-frequency distribution is $3.6^{+0.05}_{-0.08}$ Ga, which is based on 14 mapped craters in the study crater with diameter greater than 1 km (Figures S2a and S2b in Supporting Information S1). This numerical age corresponds to the late Noachian-early Hesperian epoch. Given that the FFC lacks a distinguishable ejecta blanket, doming of crater floor and shows abundant evidence for erosion, crater rim degradation, redistribution of material within the mantling units, terrain inversion, and aeolian activity, the crater size-frequency distributions may more accurately represent the

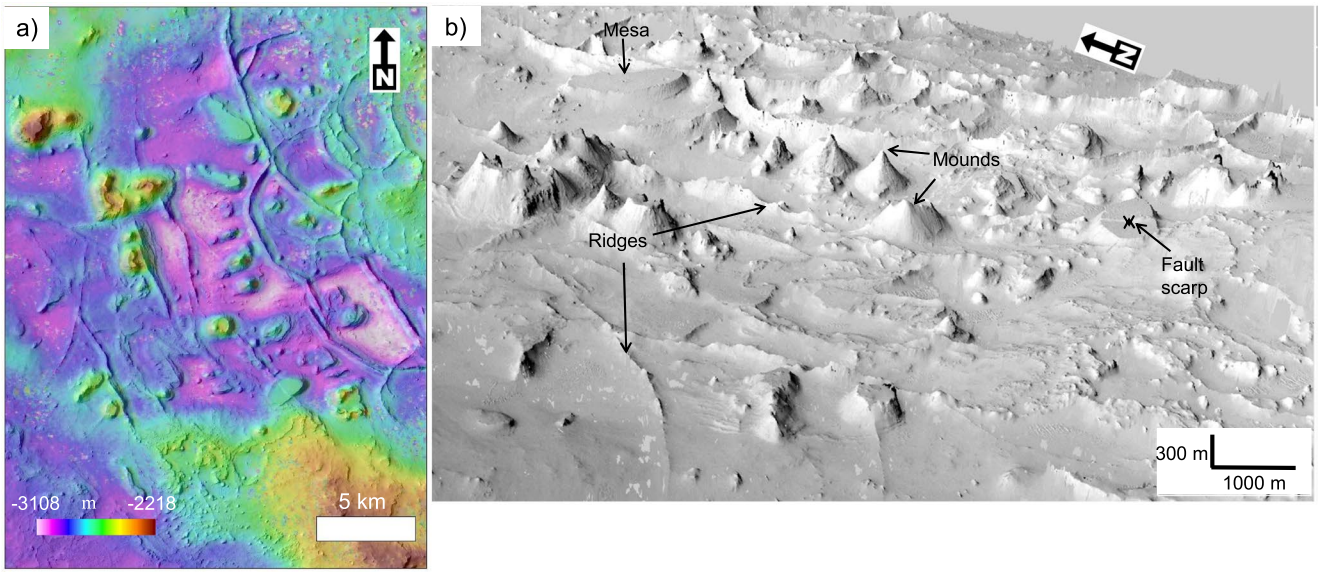

Figure 3. (a) 2D Digital Terrain Model (DTM) is overlain on Context Camera (CTX) images of the central part of the crater, showing anomalous features of variable elevation at the central portion of the crater (CTX image credit: NASA/JPL-Caltech/MSSS, Digital Elevation Model credit: USGS Astrogeology Science Center). (b) CTX-DTM-derived 3D view of central portion of the crater, showing different morphological features such as mounds, ridges, fault, mesas, and so on. CTX stereo images P21_009232_2084 and J10_04846_2083 (no vertical exaggeration) for both.

surface age and not the formation age of the landscape. A few hundred km long fluvial channel entered the study crater, likely connecting with Cerulli crater (130 km diameter, ~300 km to the southeast), breached the western rim and deposited a fan near the rim (Figures 1 and 2a–2c). The crater floor hosts layered sedimentary rocks plausibly deposited from the incised channel(s). The crater floor annulus along the rim wall is consistent with characteristics of a typical FFC; specifically, the floor is dissected by fractures and divides into mesas, ranging in size from a few hundreds of meters to ~2 km (Figure 2d). Diverse geomorphic features with a positive relief, such as mounds, linear ridges, mesas, and faults at the central part of the crater over the layered sedimentary rocks, are identifiable from shape and appearance (Figures 2c, 3a, and 3b). The isolated mesas are nearly elliptical, elongated, and irregularly shaped; mounds are semicircular to circular cone-shaped elevated features; and ridges are long and linear with very high length-to-width ratios (Figures 2c, 3a, and 3b).

3.1. Mesas

A simplified morphologic map outlines the distribution of geomorphic features observed inside the crater (Figure 2c). The floor of the interior of the crater is layered and also shows mesa-like features (Figures 4a and 4b). The isolated mesas are of near elliptical, elongated, and irregular shapes with steep flanks. Also, the plain surface on the basement unit at the central part of the crater consists of ridged plain features (Figure 4c). The terraced sedimentary layers are occasionally characterized by elliptical- or irregular-shaped positive relief features, which resemble mesas up to ~150-m high (Figures 4a, 4b, and 4d). The crater floor at the low-lying regions, where eroded, exposes nearly horizontal layers and terraces on the scarps (Figures 4a and 4b). Isolated mesa tops feature relatively high crater areal density, consistent with the original surface of the crater floor with a few inverted terrain features at its top (Figure 4d). Unlike mounds, mesas are mostly randomly distributed without preferential orientation or association with ridges (Figures 2c and 3a).

3.2. Mounds

We observe 25 conical mounds in the interior of the crater floor. Their bases are circular (up to ~1.8-km diameter) with a few exhibiting depressions at the peak, which resemble summit craters of terrestrial scoria cones (Figures 3a and 5). In this study area, mounds of significant size ($H > 200$ m) are layered and are superposed on the preexisting crater floor basement (Figure 5a). Flanks of some of the mounds are well

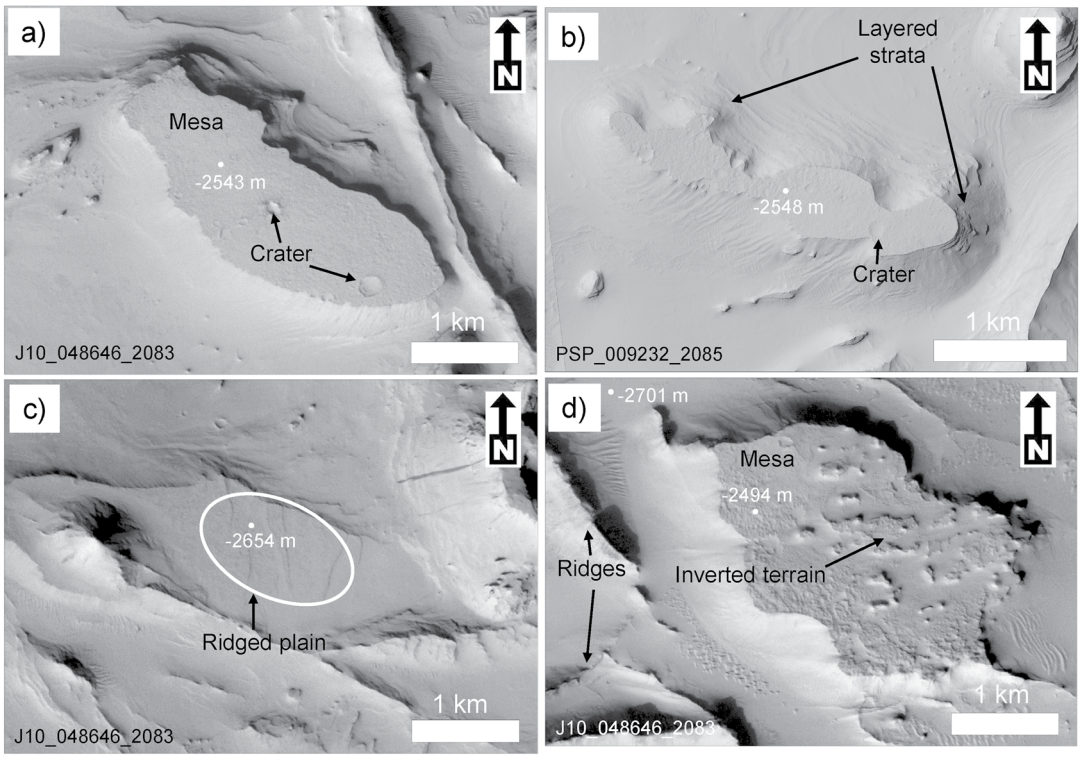

Figure 4. Basement and Mesa units. (a) An elliptical to irregular-shaped mesa with small craters on surface. (b) Preserved layered strata at the crater floor. (c) A basement block with ridged plain surface. (d) A mesa as an erosional remnant of the preexisting crater floor; inverted terrain on the mesa (Context Camera image credit: NASA/JPL-Caltech/MSSS, HiRISE image credit: NASA/JPL-Caltech/University of Arizona).

exposed and are less mantled by dust compared to other mounds. The remaining mounds have a smooth texture and show minor terraces on the flanks wherever the dust cover is thin. A few cone-shaped mounds have a flow-like feature with a downslope flow direction (Figures 5b and 5c). Qualitatively, the flow-like layers dip such that they intersect elevation contours. Meanwhile, linear ridges are associated with the mounds, which are generally underlain by the basement unit (Figure 5a). At the scale of few tens of meters, the layers of the mounds are characterized by serrated edges with triangular-shaped protrusions dipping down the flank (Figure 5a).

We have estimated the morphometry of 25 symmetric and asymmetric mounds (Table S1 in Supporting Information S1). That excludes mounds less than a 50-m height, given the limitations of CTX DTM resolution, corresponding to an ~54-m point spread function and the limited coverage (only one pair) of HiRISE DTM at the central part of the crater. Mound transect profiles reveal several features, ranging from conical shapes to summit craters (Figures 6a and 6b). The average mound heights range from 58 to 348 m (mean = 146, median = 127, and aSD = 82.5) and the average basal diameter from 290 to 1,780 m (mean = 686, median = 562, and SD = 393) with a height-to-diameter ratio of 0.144–0.309 with 4% uncertainty of the mean. The estimated standard errors of the mean in average basal diameters and average height of mounds are 12% and 11%, respectively (Figure S3 and Table S1 in Supporting Information S1). Mean slope value of the mounds is less than 35°, with 3% error, which could be subject to further uncertainties associated with the CTX-DTM generation. The mean azimuth of the mounds is NW-SE on ~127° (Figure 6c).

3.3. Ridges

Along with the mounds, a network of long, narrow linear ridges is also present in the central crater floor (Figures 3a and 7). Most of them are well exposed and exhumed, up to 20-km long and 150-m high, with varying geometries from straight to curvilinear and orthogonal types (Figures 7a–7c). The topmost part of the ridges is less dust covered and better exposed than the surroundings. The ridges are darker toned and

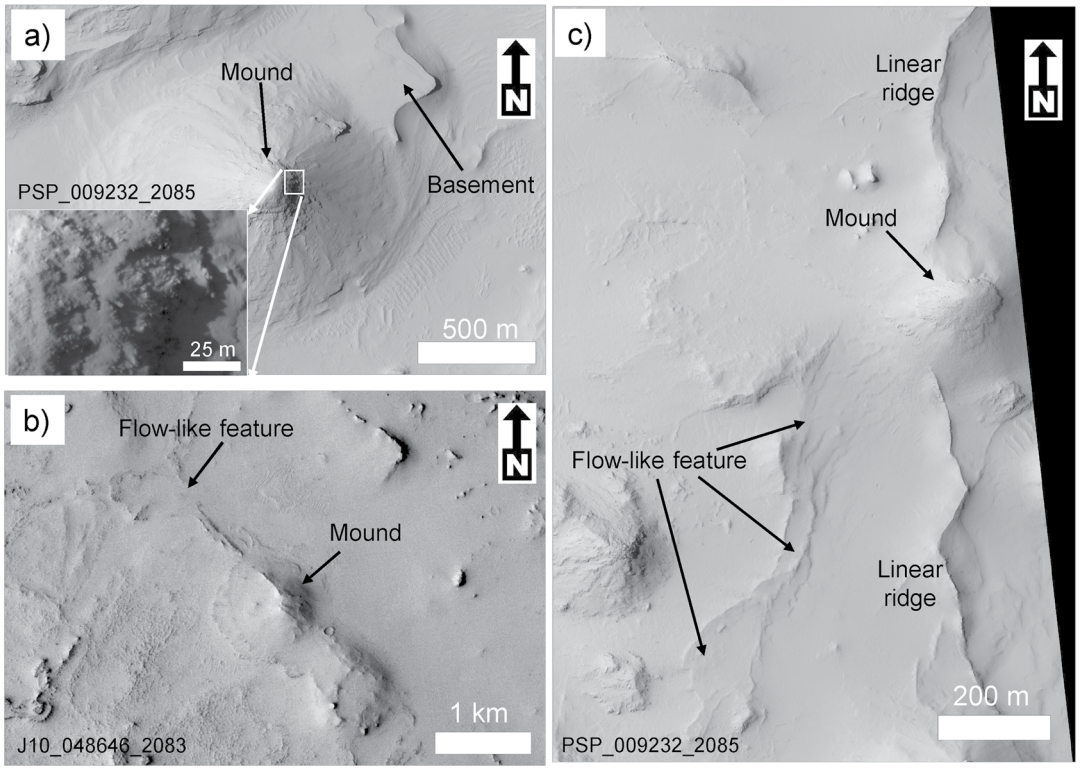

Figure 5. Mounds of the study crater. (a) Mound overlies the flat basement unit, with a rugged and serrated texture of layers exposed at top of mound, shown as an inset at the bottom left; (b) Mound flanks having flow-like features; (c) Flow-like feature near mound, possibly originated from the mound that is associated with linear ridges (Context Camera image credit: NASA/JPL-Caltech/MSSS, HiRISE image credit: NASA/JPL-Caltech/University of Arizona).

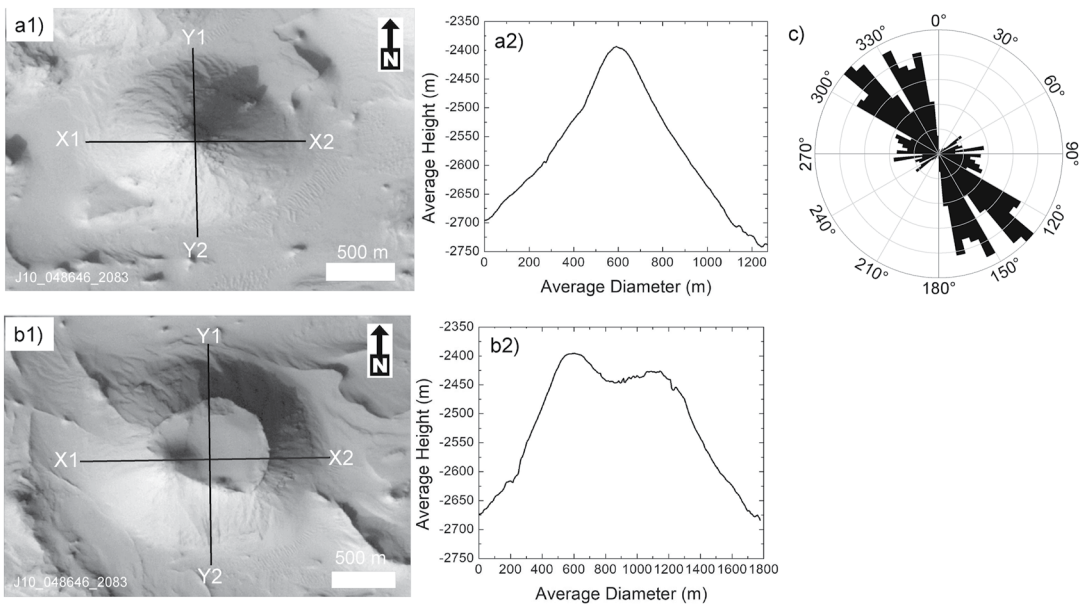

Figure 6. Average cross-sectional elevation profiles (X1-X2 and Y1-Y2) of selected mound types using Context Camera (CTX) Digital Terrain Model (CTX stereo image pair Id: P21_009232_2084 and J10_04846_2083; no vertical exaggeration). Mounds with conical shape (a1 and a2) and a crater at its summit (b1 and b2). (c) Two-point azimuth technique indicates mounds that are aligned in NW-SE direction relative to each other. See the text in Section 3.2 for details (CTX image credit: NASA/JPL-Caltech/MSSS, Digital Elevation Model credit: USGS Astrogeology Science Center).

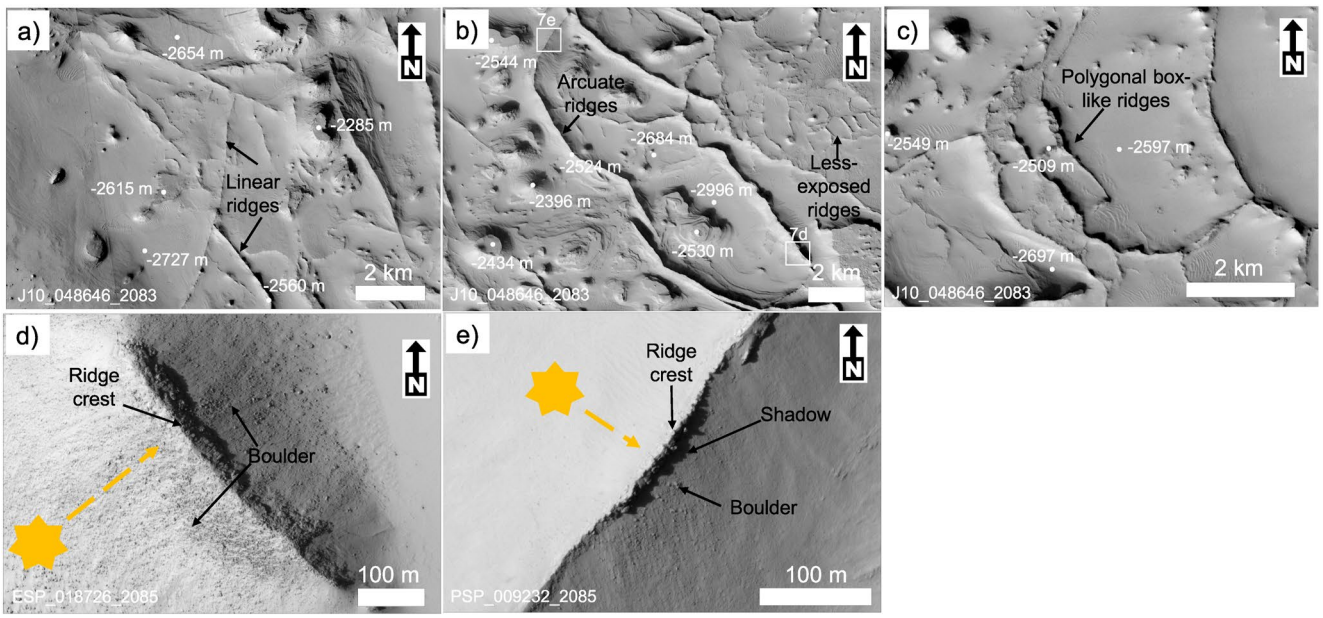

Figure 7. Linear ridges of the study crater. (a) Broad and long linear ridges; (b) arcuate or curvilinear type of linear ridges along with less-exposed small, abruptly terminated, substantially buried ridges; and (c) linear ridges with rectangular or polygonal box-like patterns. All types of ridges (a–c) having a positive relief (∼−2,520 m) nearly close to the elevation of surrounding sedimentary deposits (∼−2,530 m). (d and e) High-Resolution Imaging Science Experiment (HiRISE) images showing ridges with shedding boulders, similar to an exposed dike of Shiprock on Earth, as shown in Figure S6 in Supporting Information S1. The sun direction is shown with star marks and arrows (Context Camera image credit: NASA/JPL-Caltech/MSSS, HiRISE image credit: NASA/JPL-Caltech/University of Arizona).

appear rougher in texture than the surroundings. Another set of ridges is present in the lowermost units; these are less pronounced, narrower, discontinuous, with straight to slightly curvilinear geometries (up to 50-m high) where they are exposed (Figure 7a). The overall network of the broad and long linear ridges is nearly parallel for few kilometers in some portions, branching into smaller linear ridges, bifurcating or converging (Figure 7b), and in few occasions forming rectangular or polygonal box-like patterns (Figure 7c). The long parallel ridge group is more visually dominant than the subordinate smaller size ridge group, which is invariably associated with the parallel ridges, either branched out, merged, or connecting at a high angle or suborthogonally to the dominant parallel ridges (Figures 3a and 7a–7c). Shed boulders are present at the flanks of ridges and we could trace them at a scale of 1:1,000 to 1:2,000 on HiRISE images (Figures 7d, 7e, and S4a in Supporting Information S1). Boulder density is high along ridge flanks, which are steep, with slopes ranging from 63° to 78°, with an average of ∼67°. The shed boulder density decreases away from the ridges (Figures 7d and 7e). The dense pattern of the linear ridges can be visually characterized as either those that connected with the mounds (Figures 5c and 6b1) or those that begin or end at the mounds (Figures 5c and 8a). At the innermost central part of the study crater, where the mounds are observed, the ridge tops are at or below the elevation of the base of the mounds (Figure 3a). At the outer part of the center of the crater, the ridges are not associated with the mounds. However, the orientation of the innermost ridge-mound system and the outer ridges is uniform. There is a notable linear ridge that crosscuts at least one mesa along a steep fault plane (Figures 8b1 and 8b2). The contact between the linear ridge and the sedimentary rocks is sharp as observed in a preserved section of layered sedimentary strata and inverted terrain (Figure 8c).

Linear ridges show symmetric bell-shaped profiles for transects perpendicular to the ridge length (Figures 9a and 9b). The profiles indicate steep flanks and narrow crests. The less dust covered and more exposed part of the ridges reaches a peak of 30–40 m and roughly 100–150 m wide (Figure 9b). The height, width, and slope of the ridges range between 73–185 m, 61–118 m, and 63°–78°, respectively (Figure S4b and Tables S2–S4 in Supporting Information S1). The average spacing among the ridges is ∼4.3 ± 1.6 km (Table S5 in Supporting Information S1). The mapped ridges exhibit a prominent NW-SE orientation with ∼80% of the total length of all the ridges, while the subordinate group exists at a high angle to the dominant

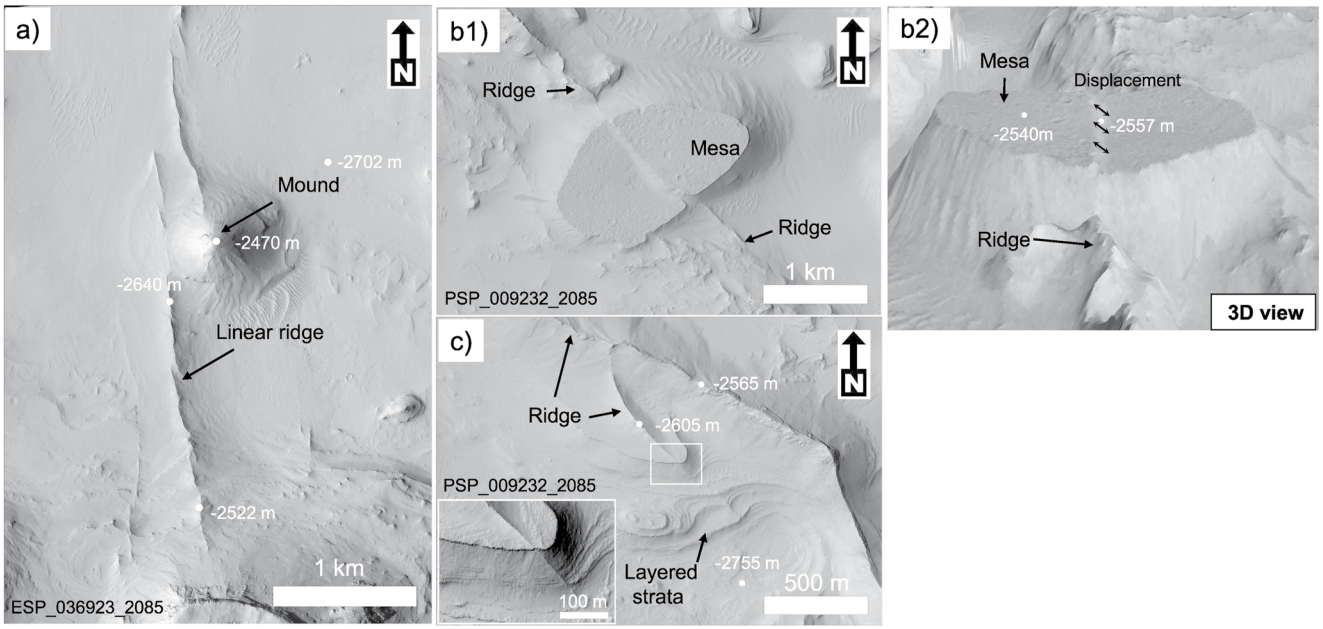

Figure 8. Crosscutting relationships among the observed geomorphic features. (a) Exhumed linear ridges in a preserved section are associated with a mound. (b1) Faulted blocks of a mesa associated with a ridge; (b2) 3D view from CTX-DTM image of the panel (b1) (no vertical exaggeration). (c) A sharp contact between ridges and layered sedimentary rocks. Sedimentary layers are crosscut by the ridges. Inset shows the zoomed-in view of the white box part (Context Camera image credit: NASA/JPL-Caltech/MSSS, High-Resolution Imaging Science Experiment image credit: NASA/JPL-Caltech/University of Arizona, Digital Elevation Model credit: USGS Astrogeology Science Center).

group and consists ~20% of the total length of the ridges (Figure 9c). The NW-SE-oriented linear ridges have parallel to subparallel distribution over several kilometers, suggesting a roughly bimodal orientation pattern with linear strikes.

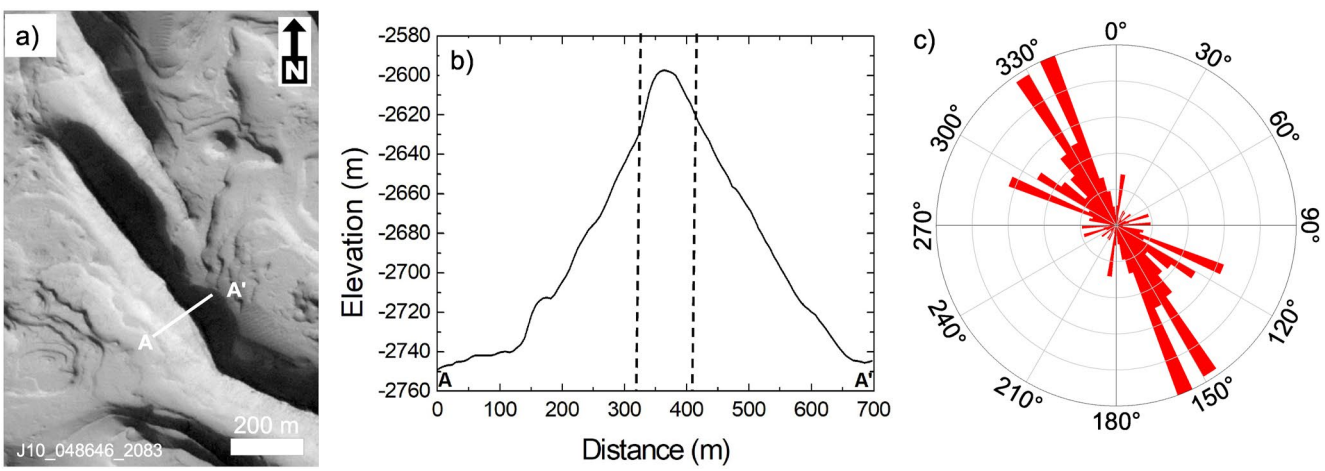

Figure 9. Morphometry of the ridges. (a) A linear ridge along which elevation profile is drawn along A-A' line. Context Camera (CTX) stereo images P21_009232_2084 and J10_04846_2083 (no exaggeration). (b) A symmetric bell-shaped topographic profile of the ridge in a cross-sectional view, showing that the ridge is ~140-m high from the surroundings. The topmost 30–40 m is relatively less dust covered and better exposed than the surroundings. The vertical dashed line is to show the dust-free topmost part of the ridge, which has a width of 100–150 m. (c) Rose diagram of the orientation of ridges in our study crater. Orientation is weighted by the corresponding length of the ridges (CTX image credit: NASA/JPL-Caltech/MSSS, Digital Elevation Model credit: USGS Astrogeology Science Center).

4. Discussion

4.1. Provenance of Linear Ridges

The kilometer-long, hundreds of meters high and wide linear ridges, consistent with sharp crest and bi-directional NW-SE trends, are of different origin than those of the other parts of Arabia Terra. In separate regions, the ridges are sinuous and typically exhibit subhorizontal meter- to decimeter-scale internal layering, suggesting they are inverted channels (cf. Davis et al., 2016; Pain et al., 2007). The lack of tributaries, obvious sinuosity, quasicircular pattern, braided pattern, paleomeander type relics, etc., of the linear ridges in our study area argues against the fluvial origin of the ridges (e.g., inverted channels or eskers). Common sedimentary ridges are sinuous in nature and circumvent large obstacles (Banks et al., 2009; Ghatan & Head, 2004; Head, 2000a, 2000b) unlike ridges in our study crater, which crosscut obstacles (Figures 5c and 8a). Furthermore, the ridges do not morphologically resemble aeolian remnant features on Mars such as transverse aeolian ridges (TARs). TARs typically occur as up to thousands of individual bedforms in a small field having narrow ridge-to-ridge spacing (mean wavelength of ~40 m; Balme et al., 2008; Nagle-McNaughton & Scuderi, 2021) and elongate in shape (Bourke et al., 2006). In our study crater, the ridges are typically elongated up to ~20 km, characterized by steep flanks and narrow crests, and the average ridge-to-ridge spacing is more than a kilometer.

The ridges within our target FFC are also unlikely to result from mineralization along the preexisting fractures or faults. For example, a small network of linear ridges formed through mineralized deposits (Mg-rich clay or calcium sulfate veins) in Gale and Eberswalde is only centimeter in scale and light toned (Crumpler et al., 2015; Golombek et al., 2012; Lévéillé et al., 2014; Nachon et al., 2014) unlike those in our study crater. Furthermore, neither Gale nor Eberswalde has been shown to exhibit ridge-mound associations. Even large vein structures (namely, boxwork) differ from the FFC's ridges. For example, the Nili Fossae ridges lack a dominant directionality (Figure S5 in Supporting Information S1) unlike those observed in our study FFC (Figure 9c). The Nili Fossae ridges (~20 m high) also fail to reach the scale of the FFC's hundreds of meter-high linear ridges, which tower above the surroundings. The ridges that we observe within the FFC are also more linear than ridges of the Nili Fossae region (Fassett & Head, 2007; Head & Mustard, 2006; Pascuzzo et al., 2019; Saper & Mustard, 2013).

Swarms of dikes and associated volcanic cones can indicate volcanic origin (Friese et al., 2013), much like the linear ridge and mound association in our studied FFC. Similar features exist in Amazonian dikes, the Huygens–Hellas region (Head et al., 2006), and the Elysium Rise-Utopia Basin region (Pedersen et al., 2010), in all of which the linear ridges are interpreted as magmatic dikes. As such, a plausible explanation for the parallel alignment of the linear ridges could be a magma ascent from underlying magmatic source forming magmatic dikes parallel to trough-bounding linear structures. Furthermore, the boulders shedding near the flanks of ridges (Figures 7d, 7e, and S4a in Supporting Information S1) are reminiscent of the exhumed radial magmatic dikes within the Medusae Fossae formation (MFF) on Mars (Kerber et al., 2017) and of the Shiprock formation on the Colorado Plateau, New Mexico (Figure S6 in Supporting Information S1). Erosion has resulted in a large population of boulders sourced from the ridges. The exhumed dikes of Shiprock (Figure S6 in Supporting Information S1) can be considered a terrestrial analog to the ridges in our study crater because of this shared morphology.

Morphologically, the few box-like polygonal ridges of our study crater differ from those presented by Kerber et al. (2017) and Pascuzzo et al. (2019), including those in Nili Fossae, Nilosyrtis, Gale crater, Sinus Meridiani, and Hellas basin. The polygonal sedimentary ridges lack a dominant orientation and constitute an irregular ridge network (Kerber et al., 2017; Pascuzzo et al., 2019). The dominant orientation of the long parallel ridge group in our studied FFC (Figure 9c) is most plausibly controlled by a preexisting fracture system induced by regional stress (explained in Section 4.5), similar to terrestrial igneous dike system (cf. Stephens et al., 2017, 2018). The shorter subordinate ridges, which are mostly oriented at a high angle to the longer parallel ridges, are typical of terrestrial volcanic fields and do not reflect the regional stress field (cf. Baer, 1991; Virgo et al., 2014). The ridge groups in our study crater and those of terrestrial analogs are arguably different from those within the volcanic domains of Utopia Planitia, where different ridge groups are not spatially related (Lanz et al., 2010). In this context, the region with the most similarity to our FFC is the MFF (Kerber et al., 2017). The similarities are: (a) broad ridges branching into smaller ridges, (b)

ridges forming a rectangular to near circular to polygonal box-like pattern, (c) ridges being parallel in some locations, (d) ridges shedding dark boulders, (e) ridges often having strikingly similar height and width, and (f) ridges are being exhumed from the surrounding terrain. These similarities are important when inferring the origin of ridges inside our study crater. The MFF similarity and its potentially pyroclastic provenance (Mandt et al., 2008) indicates that the ridges are made of more competent rocks, such as crystalline igneous materials, as opposed to the surrounding layered sedimentary rocks.

4.2. On the Occurrence of Mounds

Mounds are primarily formed through several key processes on Mars: preferential erosion of sedimentary units, volcanism, diapir-like expulsion of sediment-laden fluid, or through a mix of the two, a process known as mud volcanism. Mud volcanism versus a small-scale igneous volcanism is exemplified by the various widely distributed mounds in the northern lowlands at Chryse and Acidalia Planitia (Ann Hodges & Moore, 1979; Brož et al., 2019; Fagents et al., 2002; Farrand et al., 2005; Frey et al., 1979; Hemmi & Miyamoto, 2018; Keszthelyi et al., 2010; Komatsu et al., 2011, 2016; Lucchitta, 1981; McGowan, 2009; McNeil et al., 2021; Oehler & Allen, 2010; Tanaka, 1997; Wilson & Head, 1994). Mud volcanoes typically have smooth mound materials (Hemmi & Miyamoto, 2017). They also commonly date to the late Hesperian to middle Amazonian and are on the scale of 1–70 m in height and 40–1,400 m in diameter (Hemmi & Miyamoto, 2017, 2018). That scale is also observed in the sedimentary-layered deposits in the Firsoff, Becquerel, Kotido, and Crommelin craters of southwestern Arabia Terra, which formed from either glacial, fluvial, or eolian processes (cf. McNeil et al., 2021; Pondrelli et al., 2015; Zabrusky et al., 2012). Also, the mounds in our studied FFC lie at the central portion of the crater, which contrast to the mounds typically lying near the crater rim at the western and southwestern Arabia Terra. For example, the sedimentary mounds in South Chryse Planitia (Western Arabia Terra), which are associated with buried impact structures and formed through differential erosion after the premound layer was indurated by mineralization from groundwater (McNeil et al., 2021), are unlike the mounds of this study. This would indicate a different provenance (not mineralized or nonsedimentary) of the mounds within the FFC compared to those elsewhere in Arabia Terra. Furthermore, the FFC's observed mounds differ in both scale and morphology from typical layered sedimentary deposits and mud volcanoes.

The mounds within the studied FFC exhibit layering (Figures S7a and S7b in Supporting Information S1), which resemble volcanic layers similar to those along the flanks of Ascraeus Mons (Figure S7c in Supporting Information S1), but not those of other proposed sedimentary-layered deposits on Mars (M. A. Ivanov et al., 2014; Pondrelli et al., 2015). The sectional view of the mounds of our study crater reveals some significant dissimilarity in the structures and textures of the layering in comparison to the typical uniform and rhythmic sedimentary layers in depositional settings such as the Crommelin and Becquerel craters (Figures S7d and S7e in Supporting Information S1). In contrast to the sedimentary layers, the volcanic layers are less eroded because of welding and jointing of the more rigid crystalline materials, which occurred during the lava flow emplacement (M. A. Ivanov et al., 2014). As a result, formation of joints, fragmentation, and drop-off of lava blocks are common and result in extremely rough edges of the volcanic layers (M. A. Ivanov et al., 2014). The layers of the mounds of our study crater are characterized by rugged, serrated edges with triangular-shaped protrusions dipping down the flank, which is similar in appearance to the eroded volcanic materials (Figures 5a, S7a, and S7b in Supporting Information S1) and uncharacteristic of typical martian mud volcanoes. Moreover, the height-to-diameter ratio of the mounds ranges from 0.144 to 0.309 (Table S1 in Supporting Information S1) with an average of 0.216, a range similar to terrestrial lava domes but two orders of magnitude larger than those for typical mud volcanoes (after Table 4 of Hemmi & Miyamoto, 2018).

The mounds in the study crater are tens of meters to hundreds of meters in height and hundreds of meters basal diameter, making them too high (up to ~350 m, Table S1 in Supporting Information S1) to be the spring mounds that are, in general, low-profile landforms (Allen & Oehler, 2008; Oehler & Allen, 2010). Furthermore, the lack of preserved morphological evidence for fluid expulsion processes (Pondrelli et al., 2011, 2015) disfavors the spring deposit scenario for the formation of the mounds. Additionally, the FFC's cone-shaped mounds have flow-like features (Figures 5b and 5c), similar to many Martian (Brož & Hauber, 2012; Brož et al., 2017; Lanz et al., 2010; Meresse et al., 2008) and terrestrial (Ulrich, 1987) volcanic cones. Furthermore, the preserved flow features resemble ridged plain lavas at the basement block in our study crater

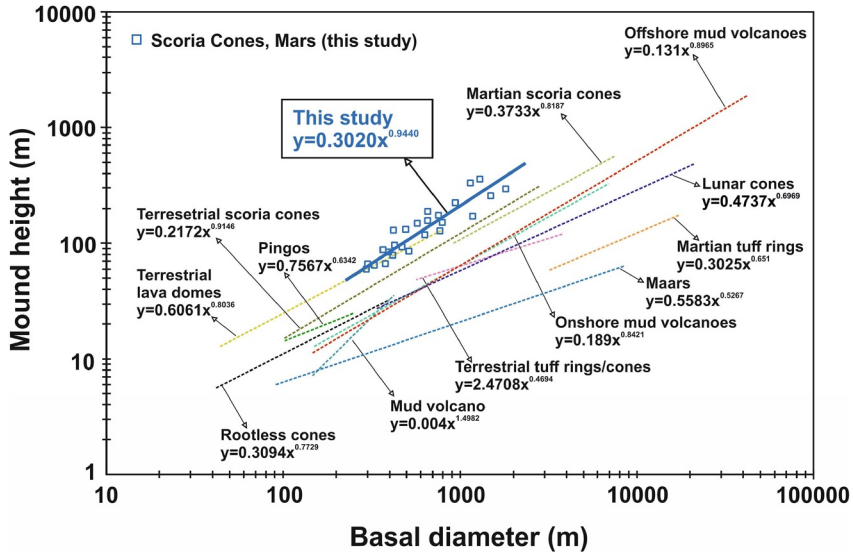

Figure 10. Height versus basal diameter plots of Martian, lunar, and terrestrial mounds (after Hemmi & Miyamoto, 2017; Wan et al., 2021). Morphometric comparison among the measured mounds (in this study) and other terrestrial analogs, log-log plots showing mound height versus basal diameter. Dashed lines represent the best linear least squares fits of parameters of each category.

(Figure 4c) and mirror the geology in Eden Patera in northern Arabia Terra (Michalski & Bleacher, 2013). Therefore, the conical mounds are most likely volcanic cones (Figures 6a and 6b), and the flow-like features associated with the mounds are the lava flows associated with the cones (Figures 5b and 5c). We also note that the FFC's mounds lack fracture patterns, making it unlikely that the mounds originated as pingos formed in periglacial environments (Balme & Gallagher, 2009; Burr et al., 2009).

We also compare mounds' slope, height versus basal diameter morphometrically with previously reported volcanic cones of Mars and Earth (Hemmi & Miyamoto, 2017, 2018). A close resemblance between the FFC and martian scoria cones, terrestrial scoria cones, and lava domes has been observed (Figure 10). However, the slope-scaling factor of the mounds in our study crater (height/width ~0.94) resembles the terrestrial (~0.91) scoria cones more than the Martian (~0.82) counterparts (Figure 10). Although earlier studies have demonstrated the similarity in shape and size between the Martian and terrestrial scoria cones (Wood, 1979), the lower gravity and atmospheric pressure on Mars than on Earth suggest that Martian scoria cones would be lower in height and larger in basal diameter than those on Earth (Brož et al., 2015; Fagents & Wilson, 1996; Parfitt & Wilson, 2008; Wilson & Head, 1994). Furthermore, the previous study focused on Amazonian aged scoria cones (Brož & Hauber, 2012; Brož et al., 2015), which are considerably younger than the mounds in our study crater (late Noachian to early Hesperian). The Martian atmosphere possibly rarefied from Noachian to the Amazonian (Wordsworth, 2016). Therefore, any volcanic cones formed on ancient Mars must have been shaped differently from the Amazonian scoria cones. In addition, the older mounds of our study crater were exposed far longer to differential erosion than the younger scoria cones of Mars, which can explain the difference in the calculated slope-scaling factor.

The high TI of mounds and ridges may indicate high density and thermal conductivity, implying resistant material than the softer surrounding layered units. In contrast, the lower values of TI of the surrounding surface materials most likely represent unconsolidated sediment or dust cover (Figure 2b). The TI observations, therefore, corroborate the igneous origin of the mounds and ridges.

There are many terrestrial analogs, where volcanic fields formed over a layered substrate. One example is in Atakor volcanic field, Algeria; a scoria cone with rugged and serrated edges and exposed dikes, which crosscut the underlying layered sediments, lies exhumed due to erosion (Figure S8a in Supporting Information S1). Sunset (SP) crater is a terrestrial analog for monogenetic volcanic cone that associated lava flow (Ulrich, 1987) in the San Francisco volcanic field north of Flagstaff, Arizona (Figure S8b in Supporting Information S1). Another terrestrial analog is Uinkaret volcanic field, in northwestern Arizona. Uinkaret,

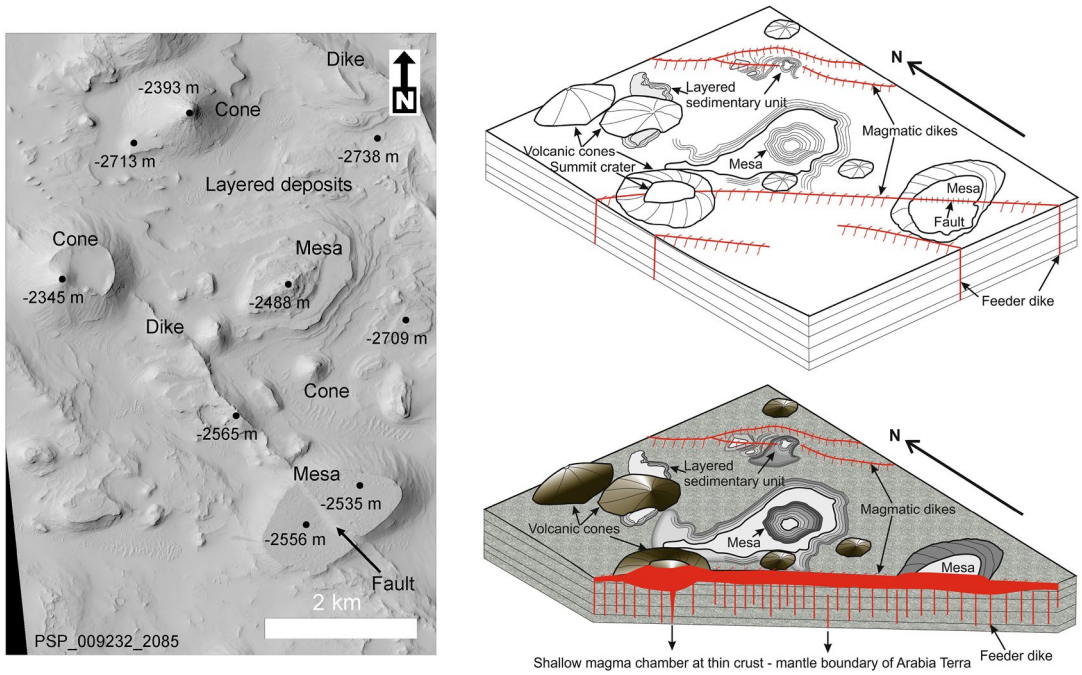

Figure 11. Left panel: Image of the interior part of the study crater with major landforms. Right panel: A schematic diagram and model for the origin of the volcanic landforms (not to scale) (High-Resolution Imaging Science Experiment image credit: NASA/JPL-Caltech/University of Arizona).

situated between fault-controlled sedimentary basement, is a N-S-trending volcanic field of cinder cones and basalt flows near the western Grand Canyon (Figure S8c in Supporting Information S1). These volcanic cones perch high atop the sedimentary rocks of the Grand Canyon (Crow et al., 2008). The terrestrial analogs, along with the combined geomorphology, morphometric analysis, stratigraphic relation, and thermal properties of the topographic features, favors our volcanic cone and magmatic dike interpretation.

4.3. Stratigraphic Relationship Among the Observed Landforms

Using the age, superposition, and crosscutting relationships described in Sections 3.1–3.3, we reconstruct the sequence of events for the stratigraphy of this FFC (Figure 11). The dense crater population and inverted relief on the basement and on the mesa tops indicate that the mesas are the parts of original crater floor (Figures 4a, 4b, and 4d). Isolated mesas with layers and sedimentary terraces are likely formed from preferential erosion of the basement unit (Figure 4b). Furthermore, dikes crosscut the mesas along steep fault planes (Figure 8b) and the underlying sedimentary rocks along sharp boundaries (Figure 8c), indicating that the dikes are younger than the mesas and sedimentary unit (Figure 11). The cones are underlain by the preexisting sedimentary unit (Figure 5a), consistent with a younger age than the crater's sedimentary deposits (Figure 11).

Although it is not possible to establish the exact superposition relation between the magmatic dikes and volcanic cones due to highly eroded landscapes, the parallel orientation of the dikes to the azimuth of the cones and similar TI between the two are consistent with a syngenetic relation. At the innermost part of the FFC interior, the dikes and cones are invariably associated with each other spatially and structurally (Figures 2a, 2b, and 3a), suggesting that the innermost dike-cone system and outer dikes were formed at different times during multiphase igneous activity, but likely from a shared source. The outer well-exposed curvilinear dikes may have emplaced in the subsurface prior to the innermost dike-cone system. The higher elevation of the outer dikes' summits compared to the base of the inner cones indicates that the cones postdate the dikes. However, the inner cone-dike system is likely cogenetic since the exposed inner dikes' summits are topographically below the bases of cones. Furthermore, interior volcanism may have volumetrically exceeded the outer annulus as the landscape would have been the deepest at the crater interior. The inner dikes were likely emplaced close to the surface from a shallow magma chamber, and further material was likely con-

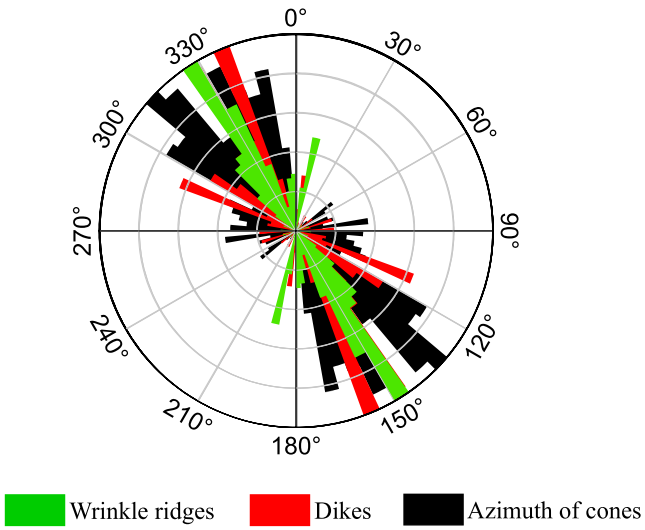

Figure 12. Orientation of the landforms (dikes and cones) in our study crater and wrinkle ridges in Arabia Terra; all showing bimodal direction tending ~NW-SE, indicating the evidence of regionally distributed tectono-volcanism.

tributed from occasional volcanic outpouring forming the volcanic cones. In either case, the cone-dike geologic unit is the younger in comparison to the layered sedimentary rocks and mesa units (Figure 11).

4.4. Possible Provenance of Igneous Features Within the Studied Impact Crater

The presence of cones and dikes at the center of a crater raises another question regarding their provenance: were the igneous features the result of impact induced magmatism or regionally expressed volcanism? Impact-induced intrusive igneous landforms, such as dikes, rarely occur within impact craters of Mars, except proximal to preexisting volcanism (B. A. Ivanov & Melosh, 2003). In order to induce local magmatism, an impact creating a >300 km diameter is needed for the typical Martian crust (Elkins-Tanton & Hager, 2005; B. A. Ivanov & Melosh, 2003). This makes impact-induced magmatism within our FFC unlikely, as its diameter is ~85 km. The impact may have exhumed ancient igneous landforms, but this would have likely disrupted any positive relief features (e.g., the cones), which we do not observe. Alternatively, Arabia Terra is an area of thinned crust (Neumann et al., 2004), over which the impact-triggered magmatism may be possible.

The coalignment of the cones and dikes suggests a putative subsurface structural control on the formation of the landforms inside the crater. Also, the nonradial orientation of the cones and dikes may indicate a NW-SE regional maximum horizontal compressive stress (Figures 6c and 9c). The NW-SE preferred orientation of large tectonic features (e.g., wrinkle ridges) of Arabia Terra (Figure 3 of Dohm et al., 2007; Figure 5 of Anderson et al., 2008) resembles the orientations of the dikes and azimuths of the cones within our study crater (Figure 12). The wrinkle ridges throughout Arabia Terra (Figures 1 and 12) may impose a typically homogeneous, regional crustal stress along the NW-SE orientation at the time of formation through propagating subsurface compressional faults and folds to the surface (Golombek et al., 2001; Hughes, 2015; Saper & Mustard, 2013). Along the steeply dipping faults or fractures, the preferred alignment of the vents and fissures is common in terrestrial volcanic fields (Le Corvec et al., 2013; Martí et al., 2016). The bidirectionality of volcanic landforms inside the studied FFC and the large tectonic features of Arabia Terra implies regional endogenic tectono-magmatism instead of exogenic impact-induced processes.

The FFCs on Mars are characterized by extensive faults, fractures, joints along with knobs, ridges, and mesas on the crater floor, mostly related to impact-cratering events (Fassett & Head, 2007; Head & Mustard, 2006). Only a few FFCs appear modified by an igneous activity (Bamberg et al., 2014; Rani et al., 2020; Schultz & Glicken, 1979), especially those occurring in volcanic provinces. In contrast, the lunar FFCs are characterized by shallow floors cut by radial, concentric, or polygonal fractures in addition to moats, ridges, and patches of mare material. Lunar craters such as these are formed by intrusive volcanism, aided by the Moon's lower crustal thickness and higher driving force of intrusion due to thermally driven viscous relaxation (e.g., Jozwiak et al., 2012, 2015). The FFCs on Mars typically lack such distinct combination of ridges and mounds at the center of the crater. Typically, the ridges inside FFCs are randomly oriented (Figure S5 in Supporting Information S1), indicating the ridges are impact-induced fracture fills. The majority of the exterior portion of the floor of our study crater close to the crater rim wall is consistent with the characteristics of a typical FFC. However, the consistent orientation of dikes and cones at the crater center with regional linear tectonic features across Arabia Terra cannot be explained by the impact event that formed the host crater. Our finding of preferential dike and cone orientation reinforces the likelihood of crustal modification in response to regional tectono-magmatism.

The crust of Arabia Terra is thinner compared to the southern highlands, more closely resembling the crustal thickness of the northern lowlands (Neumann et al., 2004). In addition to forming in a thin crust, our FFC's proposed magmatic cone-dike system's preferred orientation converges with preexisting tectonic structures, such as the wrinkle ridges of Arabia Terra. Accordingly, we hypothesize that the FFC-forming

impact (re)activated steeply dipping linear regional tectonic features, triggering the intrusion by preexisting magma bodies especially in the central crater floor where the excavation was deepest. The preferential orientation reinforces the likelihood of crustal modification in response to regional tectono-magmatism, perhaps associated with magmatism in Noachian Arabia Terra (cf. Michalski & Bleacher, 2013; Whelley et al., 2021).

5. Conclusions

Within a late Noachian-early Hesperian FFC in the East-Central Arabia Terra region, we find that the distinct geomorphic structures, primarily ridges and mounds, are of igneous origin. The dikes and cones predominantly occur at FFC's center, implying that the igneous structures formed during the syn-deformational stage of the impact or that volcanism was later rejuvenated along linear weak zones (i.e., faults and fractures). This was likely facilitated by a thinner crust proximal to the dichotomy boundary (e.g., Michalski & Bleacher, 2013). This phenomenon would also aid magmatism within our FFC. Our finding of igneous dikes and cones within the FFC may represent a broader extent of the thinned crust and could be a function of regional tectono-magmatism, an inference based on the similar orientations of linear features in the FFC and Arabia Terra. While the formation of the hypothesized volcanic structures in the FFC cannot be explained by impact induced magmatism, magmatism triggered by impact that was further facilitated by a thin crust is plausible. Furthermore, the preferential orientation and areal distribution of the volcanic features motivate future work on the flexural loading and internal shrinking of the crust of Arabia Terra during the period of late Noachian-early Hesperian.

Data Availability Statement

All the data sets can be accessed from the websites https://ode.rsl.wustl.edu/mars/, https://pilot.wr.usgs.gov/, https://www.usgs.gov/centers/astrogeology-science-center, and https://astrogeology.usgs.gov/search/map/Mars/Odyssey/THEMIS-Global-Thermal-Inertia-Mosaic/Quantitative-32-Bit/THEMIS_TI_Mosaic_Quant_00N000E_100mpp. The shape files and data sets used in this work can be downloaded from https://dx.doi.org/10.6084/m9.figshare.15035019.

Acknowledgments
A. Rani, A. Basu Sarbadhikari, and R. Sinha acknowledge the support by the Indian Space Research Organization, Department of Space, Government of India. The authors gratefully acknowledge the engineering and science teams of MRO, MGS, and Mars Odyssey for acquisition of the data sets used in this study. The authors also thank NASA AMES Stereo Pipeline and MarsSI (https://emars.univ-lyon1.fr/MarsSI/) team for developing CTX and HiRISE-DTM, an application founded by the European Union's Seventh Framework Program. This work is a part of the PhD work of A. Rani. Director PRL, Head of Planetary Science Division, PRL, and Director IIT Gandhinagar are gratefully acknowledged for constant encouragement during the work. Juan Lorenzo of Louisiana State University provided thoughtfully extensive input on stratigraphic relations among dikes and cones. The authors acknowledge Joseph Michalski and two anonymous reviewers for providing constructive and thorough reviews of the manuscript and Bradley Thomson for editorial handling.

References

Allen, C. C., & Oehler, D. Z. (2008). A case for ancient springs in Arabia Terra, Mars. *Astrobiology*, *8*(6), 1093–1112. https://doi.org/10.1089/ast.2008.0239

Amador, E. S., Allen, C. C., & Oehler, D. Z. (2010). *Regional mapping and spectral analysis of mounds in Acidalia Planitia, Mars*. 41st Lunar Planet Science Conference, Abstract #1037.

Anderson, R. C., Dohm, J. M., Haldemann, A. F. C., Pounders, E., Golombek, M., & Castano, A. (2008). Centers of tectonic activity in the eastern hemisphere of Mars. *Icarus*, *195*(2), 537–546. https://doi.org/10.1016/j.icarus.2007.12.027

Anguita, F., Anguita, J., Castilla, G., De La Casa, M. A., Domínguez, J. M., Herrera, R., et al. (1997). Arabia Terra, Mars: Tectonic and palaeoclimatic evolution of a remarkable sector of martian lithosphere. *Earth, Moon and Planets*, *77*(1), 55–72. https://doi.org/10.1023/A:1006143106970

Ann Hodges, C., & Moore, H. J. (1979). The subglacial birth of Olympus Mons and its aureoles. *Journal of Geophysical Research*, *84*, 8061–8074. https://doi.org/10.1029/JB084iB14p08061

Baer, G. (1991). Mechanisms of dike propagation in layered rocks and in massive, porous sedimentary rocks. *Journal of Geophysical Research*, *96*(B7), 911–929. https://doi.org/10.1029/91JB00844

Balme, M. R., Berman, D. C., Bourke, M. C., & Zimbelman, J. R. (2008). Transverse aeolian ridges (TARs) on Mars. *Geomorphology*, *101*(4), 703–720. https://doi.org/10.1016/j.geomorph.2008.03.011

Balme, M. R., & Gallagher, C. (2009). An equatorial periglacial landscape on Mars. *Earth and Planetary Science Letters*, *285*(1), 1–15. https://doi.org/10.1016/j.epsl.2009.05.031

Bamberg, M., Jaumann, R., Asche, H., Kneissl, T., & Michael, G. G. (2014). Floor-fractured craters on Mars—Observations and origin. *Planetary and Space Science*, *98*, 146–162. https://doi.org/10.1016/j.pss.2013.09.017

Banks, M. E., Lang, N. P., Kargel, J. S., McEwen, A. S., Baker, V. R., Grant, J. A., et al. (2009). An analysis of sinuous ridges in the southern Argyre Planitia, Mars using HiRISE and CTX images and MOLA data. *Journal of Geophysical Research*, *114*(9). https://doi.org/10.1029/2008JE003244

Bates, A., Karunatillake, S., Goossens, S., Ojha, L., & Lorenzo, J. M. (2020). *Evidence for supervolcanic resurfacing in Arabia Terra, Mars*. 51st Lunar Planet Science Conference, Abstract #1588.

Bleacher, J. E., Glaze, L. S., Greeley, R., Hauber, E., Baloga, S. M., Sakimoto, S. E. H., et al. (2009). Spatial and alignment analyses for a field of small volcanic vents south of Pavonis Mons and implications for the Tharsis province, Mars. *Journal of Volcanology and Geothermal Research*, *185*(1–2), 96–102. https://doi.org/10.1016/j.jvolgeores.2009.04.008

Bourke, M. C., Balme, M., Beyer, R. A., Williams, K. K., & Zimbelman, J. (2006). A comparison of methods used to estimate the height of sand dunes on Mars. *Geomorphology*, *81*, 440–452. https://doi.org/10.1016/j.geomorph.2006.04.023

Brož, P., Čadek, O., Hauber, E., & Rossi, A. P. (2015). Scoria cones on Mars: Detailed investigation of morphometry based on high-resolution digital elevation models. *Journal of Geophysical Research: Planets*, *120*, 1512–1527. https://doi.org/10.1002/2015JE004873

Brož, P., & Hauber, E. (2012). A unique volcanic field in Tharsis, Mars: Pyroclastic cones as evidence for explosive eruptions. *Icarus*, *218*(1), 88–99. https://doi.org/10.1016/j.icarus.2011.11.030

Brož, P., Hauber, E., van de Burgt, I., Špillar, V., & Michael, G. (2019). Subsurface sediment mobilization in the southern Chryse Planitia on Mars. *Journal of Geophysical Research: Planets*, *124*, 703–720. https://doi.org/10.1029/2018JE005868

Brož, P., Hauber, E., Wray, J., & Michael, G. (2017). Amazonian volcanism inside Valles Marineris on Mars. *Earth and Planetary Science Letters*, *473*, 122–130. https://doi.org/10.1016/j.epsl.2017.06.003

Burr, D. M., Tanaka, K. L., & Yoshikawa, K. (2009). Pingos on Earth and Mars. *Planetary and Space Science*, *57*(5–6), 541–555. https://doi.org/10.1016/j.pss.2008.11.003

Carr, M. H. (1986). Mars: A water-rich planet? *Icarus*, *68*(2), 187–216. https://doi.org/10.1016/0019-1035(86)90019-9

Christensen, P. R., Bandfield, J. L., Bell, J. F., Gorelick, N., Hamilton, V. E., Ivanov, A., et al. (2003). Morphology and composition of the surface of Mars: Mars Odyssey THEMIS results. *Science*, *300*(5628), 2056–2061. https://doi.org/10.1126/science.1080885

Connor, C. B., & Conway, M. F. (2000). Encyclopedia of volcanoes. In H. Sigurdsson (Ed.), *Basaltic volcanic fields* (pp. 331–343). Academic Press.

Crow, R., Karlstrom, K. E., McIntosh, W., Peters, L., & Dunbar, N. (2008). History of Quaternary volcanism and lava dams in western Grand Canyon based on lidar analysis, 40Ar/39Ar dating, and field studies: Implications for flow stratigraphy, timing of volcanic events, and lava dams. *Geosphere*, *4*(1), 183–206. https://doi.org/10.1130/GES00133.1

Crumpler, L. S., Arvidson, R. E., Bell, J., Clark, B. C., Cohen, B. A., Farrand, W. H., et al. (2015). Context of ancient aqueous environments on Mars from in situ geologic mapping at Endeavour Crater. *Journal of Geophysical Research: Planets*, *120*, 538–569. https://doi.org/10.1002/2014JE004699

Cushing, G. E., Titus, T. N., Soderblom, L. A., & Kirk, R. L. (2009). THEMIS high-resolution digital terrain: Topographic and thermophysical mapping of Gusev Crater, Mars. *Journal of Geophysical Research*, *114*, E07002. https://doi.org/10.1029/2008JE003292

Davis, J. M., Balme, M., Grindrod, P. M., Williams, R. M. E., & Gupta, S. (2016). Extensive Noachian fluvial systems in Arabia Terra: Implications for early martian climate. *Geology*, *44*(10), 847–850. https://doi.org/10.1130/G38247.1

Dohm, J. M., Barlow, N. G., Anderson, R. C., Williams, J. P., Miyamoto, H., Ferris, J. C., et al. (2007). Possible ancient giant basin and related water enrichment in the Arabia Terra province, Mars. *Icarus*, *190*(1), 74–92. https://doi.org/10.1016/j.icarus.2007.03.006

Dohm, J. M., Maruyama, S., Baker, V. R., Anderson, R. C., Ferris, J., & Hare, T. M. (2002). *Plate tectonism on early Mars: Diverse geological and geophysical evidence*. 33rd Lunar Planet Science Conference, Abstract #1639.

Elkins-Tanton, L. T., & Hager, B. H. (2005). Giant meteoroid impacts can cause volcanism. *Earth and Planetary Science Letters*, *239*(3–4), 219–232. https://doi.org/10.1016/j.epsl.2005.07.029

Fagents, S. A., Lanagan, P., & Greeley, R. (2002). Rootless cones on Mars: A consequence of lava-ground ice interaction. *Geological Society, London, Special Publications*, *202*, 295–317. https://doi.org/10.1144/GSL.SP.2002.202.01.15

Fagents, S. A., & Wilson, L. (1996). Numerical modeling of ejecta dispersal from transient volcanic explosions on Mars. *Icarus*, *123*(2), 284–295. https://doi.org/10.1006/icar.1996.0158

Farrand, W. H., Gaddis, L. R., & Keszthelyi, L. (2005). Pitted cones and domes on Mars: Observations in Acidalia Planitia and Cydonia Mensae using MOC, THEMIS, and TES data. *Journal of Geophysical Research*, *110*(5). https://doi.org/10.1029/2004JE002297

Fassett, C. I., & Head, J. W. (2007). Layered mantling deposits in northeast Arabia Terra, Mars: Noachian-Hesperian sedimentation, erosion, and terrain inversion. *Journal of Geophysical Research*, *112*(8). https://doi.org/10.1029/2006JE002875

Fergason, R. L., Christensen, P. R., & Kieffer, H. H. (2006). High-resolution thermal inertia derived from the ThermalEmission Imaging System (THEMIS): Thermal model and applications. *Journal of Geophysical Research*, *111*, E12004. https://doi.org/10.1029/2006JE002735

Fergason, R. L., Hare, T. M., & Laura, J. (2018). *HRSC and MOLA blended digital elevation Model at 200m v2Astrogeology PDS annex*. U.S. Geological Survey. Retrieved from http://bit.ly/HRSC_MOLA_Blend_v0

Frey, H., Lowry, B. L., & Chase, S. A. (1979). Pseudo-craters on Mars. *Journal of Geophysical Research*, *84*, 8075–8086. https://doi.org/10.1029/JB084iB14p08075

Friese, N., Frithjof, A. B., David, C. T., Lúðvík, E. G., & Siegesmund, S. (2013). From feeder dykes to scoria cones: The tectonically controlled plumbing system of the Rauðhólar volcanic chain, Northern Volcanic Zone, Iceland. *Bulletin of Volcanology*, *75*, 717. https://doi.org/10.1007/s00445-013-0717-2

Ghatan, G. J., & Head, J. W. (2004). Regional drainage of meltwater beneath a Hesperian-aged south circumpolar ice sheet on Mars. *Journal of Geophysical Research*, *109*(7). https://doi.org/10.1029/2003JE002196

Golombek, M. P., Anderson, F. S., & Zuber, M. T. (2001). Martian wrinkle ridge topography: Evidence for subsurface faults from MOLA. *Journal of Geophysical Research*, *106*(E10), 23811–23821. https://doi.org/10.1029/2000je001308

Golombek, M. P., Grant, J., Kipp, D., Vasavada, A., Kirk, R., Fergason, R., et al. (2012). Selection of the Mars Science Laboratory landing site. *Space Science Reviews*, *170*(1), 641–737. https://doi.org/10.1007/s11214-012-9916-y

Greeley, R., & Guest, J. E. (1987). *Geologic map of the eastern equatorial region of Mars*. USGS. https://doi.org/10.3133/i1802B

Head, J. W. (2000a). *Evidence for geologically recent lateral migration of volatile-rich polar layered deposits*. Second International Conference on Mars Polar Science and Exploration, abstract 4082, Lunar Planet. Sci. Inst.

Head, J. W. (2000b). *Mars south pole: Evidence for geologically recent lateral migration of volatile-rich layered deposits*. 31st Lunar Planet. Science Conference, Abstract #2036.

Head, J. W., & Mustard, J. F. (2006). Breccia dikes and crater-related faults in impact craters on Mars: Erosion and exposure on the floor of a crater 75 km in diameter at the dichotomy boundary. *Meteoritics & Planetary Sciences*, *41*(10), 1675–1690. https://doi.org/10.1111/j.1945-5100.2006.tb00444.x

Head, J. W., Wilson, L., Dickson, J., & Neukum, G. (2006). The Huygens-Hellas giant dike system on Mars: Implications for Late Noachian-Early Hesperian volcanic resurfacing and climatic evolution. *Geology*, *34*(4), 285–288. https://doi.org/10.1130/G22163.1

Hemmi, R., & Miyamoto, H. (2017). Distribution, morphology, and morphometry of circular mounds in the elongated basin of northern Terra Sirenum, Mars. *Progress in Earth and Planetary Science*, *4*(1). https://doi.org/10.1186/s40645-017-0141-x

Hemmi, R., & Miyamoto, H. (2018). High-resolution topographic analyses of mounds in southern Acidalia Planitia, mars: Implications for possible mud volcanism in submarine and subaerial environments. *Geosciences*, *8*(5), 152. https://doi.org/10.3390/geosciences8050152

Hughes, S. S. (2015). Wrinkle ridge plains. In H. Hargitai, & Á. Kereszturi (Eds.), *Encyclopedia of planetary landforms* (pp. 2331–2335). Springer. https://doi.org/10.1007/978-1-4614-3134-3_573

Hynek, B. M., & Phillips, R. J. (2001). Evidence for extensive denudation of the martian highlands. *Geology*, *29*(5), 407–410. https://doi.org/10.1130/0091-7613(2001)029<0407:efedot>2.0.co;2

Ivanov, B. A., & Melosh, H. J. (2003). Impacts do not initiate volcanic eruptions: Eruptions close to the crater. *Geology*, *31*(10), 869–872. https://doi.org/10.1130/G19669.1

Ivanov, M. A., Abdrakhimov, A. M., Guseva, E. N., Kostama, V. P., Raitala, J., Korteniemi, J., & Törmänen, T. (2014). Morphologic characteristics of volcanic and sedimentary sequences on Mars. *Solar System Research*, *48*(2), 130–138. https://doi.org/10.1134/S003809461402004X

Jozwiak, L. M., Head, J. W., & Wilson, L. (2015). Lunar floor-fractured craters as magmatic intrusions: Geometry, modes of emplacement, associated tectonic and volcanic features, and implications for gravity anomalies. *Icarus*, *248*, 424–447. https://doi.org/10.1016/j.icarus.2014.10.052

Jozwiak, L. M., Head, J. W., Zuber, M. T., Smith, D. E., & Neumann, G. A. (2012). Lunar floor-fractured craters: Classification, distribution, origin and implications for magmatism and shallow crustal structure. *Journal of Geophysical Research*, *117*(E11). https://doi.org/10.1029/2012JE004134

Kerber, L., Dickson, J. L., Head, J. W., & Grosfils, E. B. (2017). Polygonal ridge networks on Mars: Diversity of morphologies and the special case of the Eastern Medusae Fossae Formation. *Icarus*, *281*, 200–219. https://doi.org/10.1016/j.icarus.2016.08.020

Keszthelyi, L. P., Jaeger, W. L., Dundas, C. M., Martínez-Alonso, S., McEwen, A. S., & Milazzo, M. P. (2010). Hydrovolcanic features on Mars: Preliminary observations from the first Mars year of HIRISE imaging. *Icarus*, *205*, 211–229. https://doi.org/10.1016/j.icarus.2009.08.020

Komatsu, G., Okubo, C. H., Wray, J. J., Ojha, L., Cardinale, M., Murana, A., et al. (2016). Small edifice features in Chryse Planitia, Mars: Assessment of a mud volcano hypothesis. *Icarus*, *268*, 56–75. https://doi.org/10.1016/j.icarus.2015.12.032

Komatsu, G., Ori, G. G., Cardinale, M., Dohm, J. M., Baker, V. R., Vaz, D. A., et al. (2011). Roles of methane and carbon dioxide in geological processes on Mars. *Planetary and Space Science*, *59*(2–3), 169–181. https://doi.org/10.1016/j.pss.2010.07.002

Lanz, J. K., Wagner, R., Wolf, U., Kröchert, J., & Neukum, G. (2010). Rift zone volcanism and associated cinder cone field in Utopia Planitia, Mars. *Journal of Geophysical Research*, *115*, E12019. https://doi.org/10.1029/2010JE003578

Le Corvec, N., Spörli, K., Rowland, J., & Lindsay, J. (2013). Spatial distribution and alignments of volcanic centers: Clues to the formation of monogenetic volcanic fields. *Earth-Science Reviews*, *124*, 96–114. https://doi.org/10.1016/j.earscirev.2013.05.005

Léveillé, R. J., Bridges, J., Wiens, R. C., Mangold, N., Cousin, A., Lanza, N., et al. (2014). Chemistry of fracture-filling raised ridges in Yellowknife Bay, Gale Crater: Window into past aqueous activity and habitability on Mars. *Journal of Geophysical Research: Planets*, *119*(11), 2398–2415. https://doi.org/10.1002/2014JE004620

Lozac'h, L., Quantin-Nataf, C., Allemand, P., Bultel, B., Clenet, H., Harrisson, S., et al. (2015). *MARSSI: A distributed information system for managing data of the surface of mars* (pp. 2–3). Second Planetary Data Workshop.

Lucchitta, B. K. (1981). Mars and Earth: Comparison of cold-climate features. *Icarus*, *45*, 264–303. https://doi.org/10.1016/0019-1035(81)90035-X

Lutz, T. M. (1986). An analysis of the orientations of large-scale crustal structures: A statistical approach based on areal distributions of pointlike features. *Journal of Geophysical Research*, *91*(B1), 421–434. https://doi.org/10.1029/JB091iB01p00421

Malin, M. C., Bell, J. F., Cantor, B. A., Caplinger, M. A., Calvin, W. M., Clancy, R. T., et al. (2007). Context Camera Investigation on board the Mars Reconnaissance Orbiter. *Journal of Geophysical Research*, *112*(5). https://doi.org/10.1029/2006JE002808

Mandt, K. E., de Silva, S. L., Zimbelman, J. R., & Crown, D. A. (2008). Origin of the Medusae Fossae Formation, Mars: Insights from a synoptic approach. *Journal of Geophysical Research*, *113*(E12). https://doi.org/10.1029/2008JE003076

Martí, J., López, C., Bartolini, S., Becerril, L., & Geyer, A. (2016). Stress Controls of Monogenetic Volcanism: A Review. *Frontiers of Earth Science*, *4*(106). https://doi.org/10.3389/feart.2016.00106

McEwen, A. S., Eliason, E. M., Bergstrom, J. W., Bridges, N. T., Hansen, C. J., Delamere, W. A., et al. (2007). Mars reconnaissance orbiter's high resolution imaging science experiment (HiRISE). *Journal of Geophysical Research*, *112*(5). https://doi.org/10.1029/2005JE002605

McGill, G. E. (2000). Crustal history of north central Arabia Terra, Mars. *Journal of Geophysical Research*, *105*(E3), 6945–6959. https://doi.org/10.1029/1999JE001175

McGowan, E. (2009). Spatial distribution of putative water related features in southern Acidalia/Cydonia Mensae, Mars. *Icarus*, *202*, 78–89. https://doi.org/10.1016/j.icarus.2009.02.024

McNeil, J. D., Fawdon, P., Balme, M. R., & Coe, A. L. (2021). Morphology, morphometry and distribution of isolated landforms in southern Chryse Planitia, Mars. *Journal of Geophysical Research: Planets*, *126*(5). https://doi.org/10.1029/2020JE006775

Meresse, S., Costard, F., Mangold, N., Masson, P., & Neukum, G. (2008). Formation and evolution of the chaotic terrains by subsidence and magmatism: Hydraotes Chaos, Mars. *Icarus*, *194*(2), 487–500. https://doi.org/10.1016/j.icarus.2007.10.023

Michael, G. G. (2013). Planetary surface dating from crater size-frequency distribution measurements: Multiple resurfacing episodes and differential isochron fitting. *Icarus*, *226*(1), 885–890. https://doi.org/10.1016/j.icarus.2013.07.004

Michalski, J. R., & Bleacher, J. E. (2013). Supervolcanoes within an ancient volcanic province in Arabia Terra, Mars. *Nature*, *502*(7469), 47–52. https://doi.org/10.1038/nature12482

Nachon, M., Clegg, S. M., Mangold, N., Schröder, S., Kah, L. C., Dromart, G., et al. (2014). Calcium sulfate veins characterized by ChemCam/Curiosity at Gale crater, Mars. *Journal of Geophysical Research: Planets*, *119*, 1991–2016. https://doi.org/10.1002/2013JE004588

Nagle-McNaughton, T. P., & Scuderi, L. A. (2021). A geomorphological case for multistage evolution of transverse aeolian ridges. *Planetary and Space Science*, *200*, 105192. https://doi.org/10.1016/j.pss.2021.105192

Neumann, G. A., Zuber, M. T., Wieczorek, M. A., McGovern, P. J., Lemoine, F. G., & Smith, D. E. (2004). Crustal structure of Mars from gravity and topography. *Journal of Geophysical Research*, *109*(8). https://doi.org/10.1029/2004JE002262

Noe Dobrea, E. Z., Bishop, J. L., McKeown, N. K., Fu, R., Rossi, C. M., Michalski, J. R., et al. (2010). Mineralogy and stratigraphy of phyllosilicate-bearing and dark mantling units in the greater Mawrth Vallis/west Arabia Terra area: Constraints on geological origin. *Journal of Geophysical Research*, *115*. https://doi.org/10.1029/2009je003351

Oehler, D. Z., & Allen, C. C. (2010). Evidence for pervasive mud volcanism in Acidalia Planitia, Mars. *Icarus*, *208*(2), 636–657. https://doi.org/10.1016/j.icarus.2010.03.031

Pain, C. F., Clarke, J. D. A., & Thomas, M. (2007). Inversion of relief on Mars. *Icarus*, *190*(2), 478–491. https://doi.org/10.1016/j.icarus.2007.03.017

Parfitt, L., & Wilson, L. (2008). *Fundamentals of physical volcanology*. John Wiley & Sons.

Pascuzzo, A. C., Mustard, J. F., Kremer, C. H., & Ebinger, E. (2019). The formation of irregular polygonal ridge networks, Nili Fossae, Mars: Implications for extensive subsurface channelized fluid flow in the Noachian. *Icarus*, *319*, 852–868. https://doi.org/10.1016/j.icarus.2018.10.020

Pedersen, G. B. M., Head, J. W., & Wilson, L. (2010). Formation, erosion and exposure of Early Amazonian dikes, dike swarms and possible subglacial eruptions in the Elysium Rise/Utopia Basin Region, Mars. *Earth and Planetary Science Letters*, *294*(3–4), 424–439. https://doi.org/10.1016/j.epsl.2009.08.010

Pondrelli, M., Rossi, A. P., Le Deit, L., Fueten, F., van Gasselt, S., Glamoclija, M., et al. (2015). Equatorial layered deposits in Arabia Terra, Mars: Facies and process variability. *Bulletin of the Geological Society of America*, *127*(7–8), 1064–1089. https://doi.org/10.1130/B31225.1

Pondrelli, M., Rossi, A. P., Ori, G. G., van Gasselt, S., Praeg, D., & Ceramicola, S. (2011). Mud volcanoes in the geologic record of Mars: The case of Firsoff crater. *Earth and Planetary Science Letters*, *304*(3–4), 511–519. https://doi.org/10.1016/j.epsl.2011.02.027

Quantin-Nataf, C., Lozac'h, L., Thollot, P., Loizeau, D., Bultel, B., Fernando, J., et al. (2018). MarsSI: Martian surface data processing information system. *Planetary and Space Science*, *150*, 157–170. https://doi.org/10.1016/j.pss.2017.09.014

Rani, A., Basu Sarbadhikari, A., Sinha, R. K., Karunatillake, S., Komatsu, G., & Bates, A. (2020). *Mounds and ridges inside a floor-fractured crater in central eastern Arabia Terra*. 51st Lunar and Planetary Institute Science Conference, Abstracts # 1955.

Roberts, K. S., Davies, R. J., Stewart, S. A., & Tingay, M. (2011). Structural controls on mud volcano vent distributions: Examples from Azerbaijan and Lusi, east Java. *Journal of the Geological Society*, *168*(4), 1013–1030. https://doi.org/10.1144/0016-76492010-158

Rodriguez, J. A. P., Tanaka, K. L., Yamamoto, A., Berman, D. C., Zimbelman, J. R., Kargel, J. S., et al. (2010). The sedimentology and dynamics of crater-affiliated wind streaks in western Arabia Terra, Mars and Patagonia, Argentina. *Geomorphology*, *121*(1–2), 30–54. https://doi.org/10.1016/j.geomorph.2009.07.020

Saper, L., & Mustard, J. F. (2013). Extensive linear ridge networks in Nili Fossae and Nilosyrtis, Mars: Implications for fluid flow in the ancient crust. *Geophysical Research Letters*, *40*(2), 245–249. https://doi.org/10.1002/grl.50106

Schultz, P. H., & Glicken, H. (1979). Impact crater and basin control of igneous processes on Mars. *Journal of Geophysical Research*, *84*(9), 8033–8047. https://doi.org/10.1029/JB084iB14p08033

Shean, D. E., Fahle, J., Malin, M. C., Edwards, L. J., & Posiolova, L. (2011). *MRO CTX stereo image processing and preliminary DEM quality assessment*. 46th Lunar and Planetary Institute Science Conference, Abstracts # 2646.

Silvestro, S., Vaz, D. A., Fenton, L. K., & Geissler, P. E. (2011). Active aeolian processes on Mars: A regional study in Arabia and Meridiani Terrae. *Geophysical Research Letters*, *38*(20), 2–7. https://doi.org/10.1029/2011GL048955

Stephens, T. L., Walker, R. J., Healy, D., Bubeck, A., & England, R. W. (2018). Mechanical models to estimate the paleostress state from igneous intrusions. *Solid Earth*, *9*, 847–858. https://doi.org/10.5194/se-9-847-2018

Stephens, T. L., Walker, R. J., Healy, D., Bubeck, A., England, R. W., & McCaffrey, K. J. W. (2017). Igneous sills record far-field and near-field stress interactions during volcano construction: Isle of Mull, Scotland. *Earth and Planetary Science Letters*, *478*, 159–174. https://doi.org/10.1016/j.epsl.2017.09.003

Tanaka, K. L. (1997). Sedimentary history and mass flow structures of Chryse and Acidalia Planitiae, Mars. *Journal of Geophysical Research*, *102*, 4131–4149. https://doi.org/10.1029/96JE02862

Tanaka, K. L., Skinner, J. A., Dohm, J. M., Irwin, R. P., & Kolb, E. J. (2014). *Pamphlet accompanies map* (p. 3292).

Ulrich, G. E. (1987). SP Mountain cinder cone and lava flow, northern Arizona. In S. S. Beus (Ed.), *Centennial field guide volume 2 rocky mountain section of the* (pp. 385–388). Geological Society of America.

Virgo, S., Abe, S., & Urai, J. L. (2014). The evolution of crack seal vein and fracture networks in an evolving stress field: Insights from Discrete Element Models of fracture sealing. *Journal of Geophysical Research: Solid Earth*, *119*, 8708–8727. https://doi.org/10.1002/2014JB011520

Wadge, G., & Cross, A. (1988). Quantitative methods for detecting aligned points: An application to the volcanic vents of the Michoacan-Guanajuato volcanic field, Mexico. *Geology*, *16*(9), 815–818. https://doi.org/10.1130/0091-7613(1988)016<0815:qmfdap>2.3.co;2

Wan, S., Qiao, L., & Ling, Z. C. (2021). *Morphometry, Morphology and topography of volcanic cones in marius hill, the Moon*. 52nd Lunar Planet Science Conference, Abstract #1958.

Whelley, P., Matiella Novak, A., Richardson, J., Bleacher, J., Mach, K., & Smith, R. N. (2021). Stratigraphic evidence for early martian explosive volcanism in Arabia Terra. *Geophysical Research Letters*, *48*(15), 1–12. https://doi.org/10.1029/2021GL094109

Williams, R. M. E., Moersch, J. E., & Fergason, R. L. (2018). Thermophysical properties of martian fluvial sinuous ridges: Inferences on "inverted channel" induration agent. *Earth and Space Science*, *5*, 516–528. https://doi.org/10.1029/2018EA000402

Wilson, L., & Head, J. W. (1994). Mars: Review and analysis of volcanic eruption theory and relationships to observed landforms. *Reviews of Geophysics*, *32*(3), 221–263. https://doi.org/10.1029/94RG01113

Wood, C. A. (1979). *Cinder cones on Earth, Moon and Mars*. 10th Lunar and Planetary Institute Science Conference, Abstract 1370–1372.

Wordsworth, R. D. (2016). The climate of early Mars. *Annual Review of Earth and Planetary Sciences*, *44*, 381–408. https://doi.org/10.1146/annurev-earth-060115-012355

Zabrusky, K., Andrews-Hanna, J. C., & Wiseman, S. M. (2012). Reconstructing the distribution and depositional history of the sedimentary deposits of Arabia Terra, Mars. *Icarus*, *220*(2), 311–330. https://doi.org/10.1016/j.icarus.2012.05.007

Zeilnhofer, M. F., Chandler, C. O., & Barlow, N. G. (2018). Evidence of low-latitude fluvial and glacial activity during the martian Amazonian era. *Research Notes of the AAS*, *2*(3), 118. https://doi.org/10.3847/2515-5172/aad09d

References From the Supporting Information

Ebinger, E. K., & Mustard, J. F. (2015). *Linear ridges in the Nilosyrtis region of Mars: Implications for subsurface fluid flow*. 46th Lunar and Planetary Science Conference, Abstract #2034.

Ebinger, E. K., & Mustard, J. F. (2016). *Classification of curvilinear ridges in the Nilosyrtis highlands of Mars*. 47th Lunar and Planetary Science Conference, Abstract #2731.

Hartmann, W. K., & Neukum, G. (2001). Cratering chronology and the evolution of Mars. *Space Science Reviews*, *96*(1–4), 165–194. https://doi.org/10.1023/A:1011945222010

Ivanov, B. A. (2001). Mars/Moon cratering rate ratio estimates. *Space Science Reviews*, *96*(1–4), 87–104. https://doi.org/10.1023/A:1011941121102

Kneissl, T., Van Gasselt, S., & Neukum, G. (2011). Map-projection-independent crater size-frequency determination in GIS environments—New software tool for ArcGIS. *Planetary and Space Science*, *59*(11–12), 1243–1254. https://doi.org/10.1016/j.pss.2010.03.015

Michael, G. G., & Neukum, G. (2010). Planetary surface dating from crater size-frequency distribution measurements: Partial resurfacing events and statistical age uncertainty. *Earth and Planetary Science Letters*, *294*(3–4), 223–229. https://doi.org/10.1016/j.epsl.2009.12.041

Michael, G. G., Platz, T., Kneissl, T., & Schmedemann, N. (2012). Planetary surface dating from crater size-frequency distribution measurements: Spatial randomness and clustering. *Icarus*, *218*(1), 169–177. https://doi.org/10.1016/j.icarus.2011.11.033